NANO LETTERS

Letter

pubs.acs.org/NanoLett

Organic–Inorganic Heterointerfaces for Ultrasensitive Detection of Ultraviolet Light

Dali Shao,[†] Jian Gao,[‡] Philippe Chow,[‡] Hongtao Sun,[§] Guoqing Xin,[§] Prachi Sharma,[†] Jie Lian,[§] Nikhil A. Koratkar,*[,‡,§] and Shayla Sawyer*[,†]

[†]Department of Electrical, Computer, and Systems Engineering, [‡]Department of Materials Science and Engineering, and [§]Department of Mechanical, Aerospace, and Nuclear Engineering, Rensselaer Polytechnic Institute, 110 8th Street, Troy, New York 12180, United States

Supporting Information

ABSTRACT: The performance of graphene field-effect transistors is limited by the drastically reduced carrier mobility of graphene on silicon dioxide (SiO_2) substrates. Here we demonstrate an ultrasensitive ultraviolet (UV) phototransistor featuring an organic self-assembled monolayer (SAM) sandwiched between an inorganic ZnO quantum dots decorated graphene channel and a conventional SiO_2/Si substrate. Remarkably, the room-temperature mobility of the chemical-vapor-deposition grown graphene channel on the SAM is an order-of-magnitude higher than on SiO_2, thereby drastically reducing electron transit-time in the channel. The resulting recirculation of electrons (in the graphene channel) within the lifetime of the photogenerated holes (in the ZnO) increases the photoresponsivity and gain of the transistor to $\sim 10^8$ A/W and $\sim 3 \times 10^9$, respectively with a UV to visible rejection ratio of $\sim 10^3$. Our UV photodetector device manufacturing is also compatible with current semiconductor processing, and suitable for large volume production.

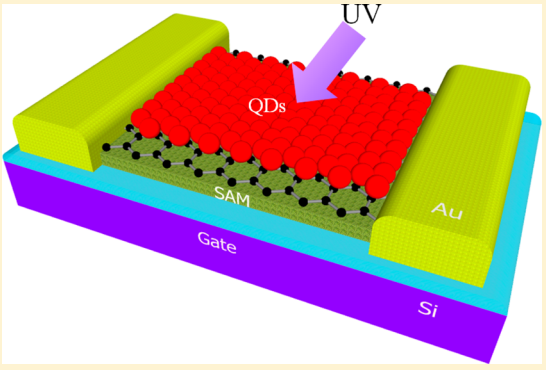

KEYWORDS: *Ultraviolet photodetector, graphene, heterointerface, ZnO quantum dots, gain*

Graphene based field-effect transistors (FETs)[1−3] are promising for various applications including photodetection, gas sensing, and bioelectronics, which greatly benefit from graphene's notably high mobility, flexibility, and ultrathin nature.[4,5] Indeed, extraordinarily high carrier mobilities of up to ~200,000 $cm^2\ V^{-1}\ s^{-1}$ have been reported in suspended graphene samples at 5 K.[6] Unfortunately, graphene transistors fabricated on dielectric substrates (such as SiO_2) exhibit a field-effect mobility that is orders of magnitude lower than that of the free-standing graphene, which significantly reduces the performance of such graphene-based FETs.[7−11] The reduced mobility of graphene on SiO_2 originates from charged impurity scattering,[7,8] extrinsic scattering by surface phonons,[9] resonant scattering from atomic scale defects,[10] and corrugation by residual adsorbates.[11] In order to realize the full potential of graphene for next generation electronic and optoelectronic devices, it is crucial that the harmful effects of the substrate be minimized so that the high mobility achieved in free-standing graphene can be largely preserved.

For device applications, nonpolar substrates have been suggested to be beneficial,[6] yet finding such materials remains a challenge. For example, scalable methods of deploying hexagonal boron nitride such as chemical vapor deposition result in significantly wrinkled and defective films[12] that do not provide the same level of benefit as mechanically exfoliated boron nitride in microelectronics applications. Recent studies have shown that insertion of an organic self-assembled monolayer (SAM) between SiO_2 and graphene can significantly improve the carrier mobility of graphene.[13−15] The SAM acts as a spacer that physically separates and electrically decouples the graphene sheet from the SiO_2 surface. However, so far the majority of work has focused on mechanically exfoliated graphene that does not provide a viable route to practical devices. Further, there is no report of graphene phototransistors employing SAMs for high-performance photosensing applications. In this study, we have utilized a 10-decyltrichlorosilane SAM to support a chemical vapor deposition (CVD) grown monolayer graphene sheet on a SiO_2/Si substrate. We report an order of magnitude increase in the room-temperature carrier mobility of the graphene sheet from ~1,120 $cm^2\ V^{-1}\ s^{-1}$ without the SAM to ~10,800 $cm^2\ V^{-1}\ s^{-1}$ with the SAM. We further deposit ZnO quantum dots (QDs) on the SAM-supported graphene and construct a phototransistor[16−18] device for ultraviolet (UV) detection. The extraordinarily high carrier mobility of the graphene–SAM heterointerface boosts the photoconductive gain of our hybrid phototransistor by drastically reducing the electron transit time within the FET channel. The phototransistor demonstrates a

Received: January 29, 2015
Revised: April 22, 2015
Published: May 4, 2015

DOI: 10.1021/acs.nanolett.5b00380
Nano Lett. 2015, 15, 3787−3792

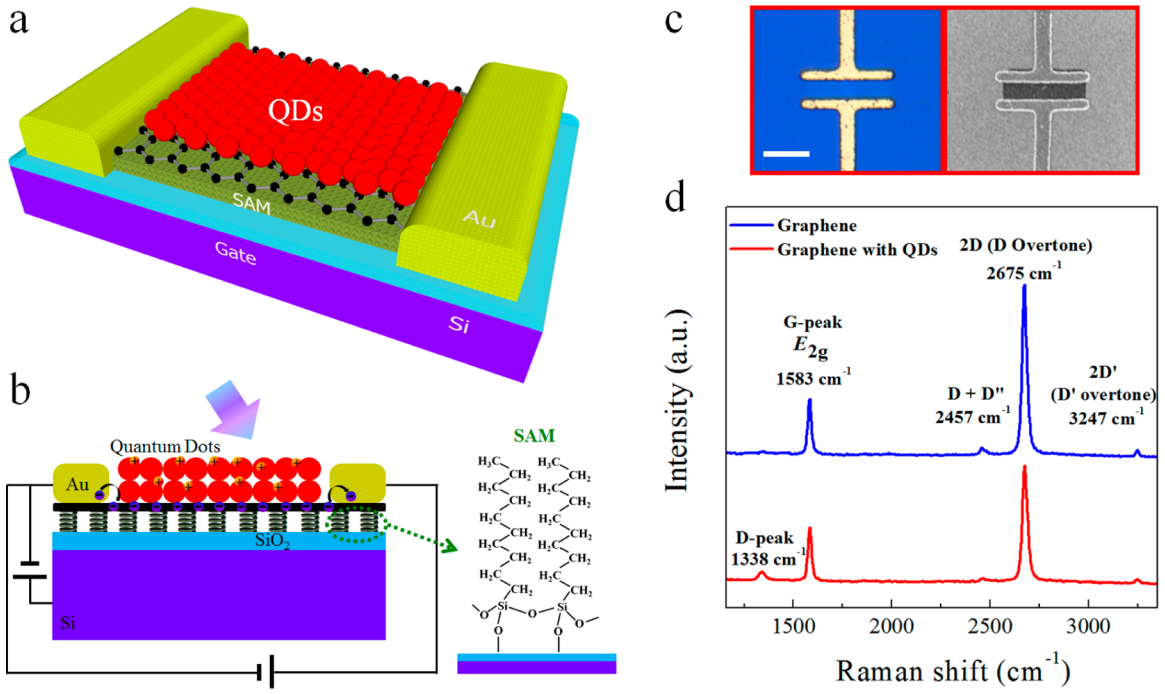

Figure 1. (a) Three-dimensional schematic illustration of the hybrid phototransistor device. (b) Side view of the hybrid phototransistor with illustration of the molecular structure of the organic self-assembled monolayer (SAM) support. (c) Optical microscopy (left) and scanning electron microscopy (right) images of the chemical vapor deposition grown monolayer graphene used in this study in contact with the gold electrodes, forming the phototransistor. The scale bar in the figure corresponds to ~50 μm. (d) Raman spectrum of the monolayer graphene on SAM/SiO_2 before (blue) and after (red) deposition of ZnO QDs.

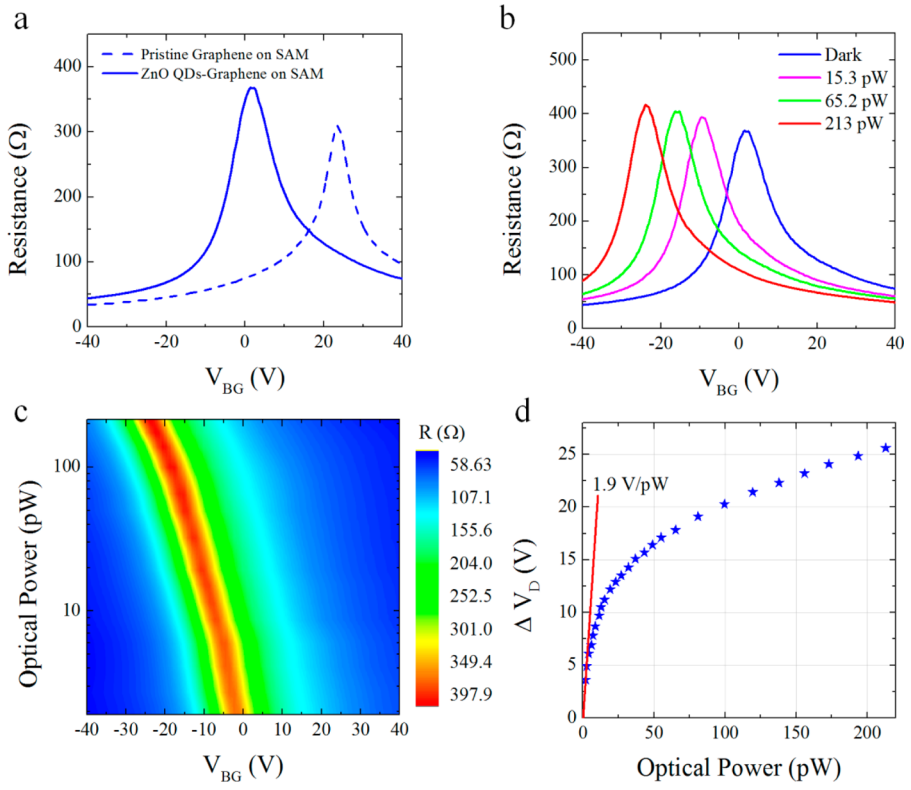

Figure 2. (a) Channel resistance of the pristine graphene and the ZnO QDs-graphene measured under dark environment. (b) Channel resistance of the ZnO QDs-graphene hybrid phototransistor as a function of back-gate voltage with varying illuminating power (wavelength: 335 nm). Increasing the illumination leads to a shift of the Dirac point to lower back-gate voltage; this indicates transfer of electrons from the ZnO QDs to the graphene channel. (c) Channel resistance as a function of illuminating power and back-gate voltage. (d) Shift of Dirac point as a function of the illuminating power on the hybrid phototransistor.

DOI: 10.1021/acs.nanolett.5b00380
Nano Lett. 2015, 15, 3787−3792

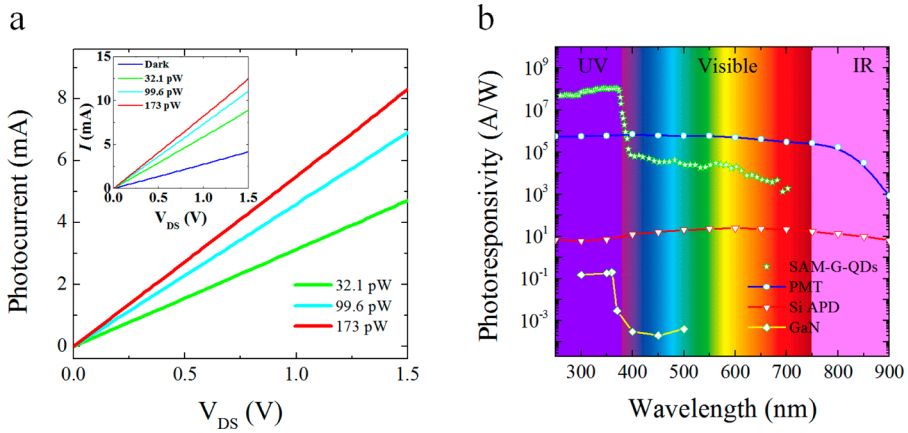

Figure 3. (a) Photocurrent of the hybrid phototransistor as a function of drain−source voltage measured under varying illuminating power. Inset: total current of the device (photocurrent + dark current). (b) Photoresponsivity spectrum of our hybrid UV phototransistor (SAM-G-QDs) in comparison with commercial PMT, Si APD and GaN photodetectors.

photoresponsivity of ~10^8 A/W and a gain of ~3×10^9 in the UV region with an excellent UV to visible rejection ratio (~1000). To our knowledge this is the highest photoresponsivity and gain that has been reported in the literature for UV sensing and is at least an order of magnitude better than the performance of the phototransistor devices without the SAM. The specific detectivity of our device is ~5.1×10^{13} Jones at 368 nm at room temperature. For commercial photodetectors, only photomultiplier tube (PMT) has a higher detectivity than our device (in the UV region). However, PMT has several obvious disadvantages, including large size, high cost, and the requirement for a high-voltage power supply (typically above 1 kV).

In this study, we also provide a detailed physical model to explain the internal gain mechanism in the heterostructure, which will help to further understand the working mechanism and improve the performance of such graphene-based phototransistors. In addition to the high sensitivity, the fabrication process for our phototransistor device is scalable because we use large-area CVD graphene and SAM deposition at the wafer scale on Si/SiO_2 substrates. This process is compatible with semiconductor processing and could potentially be scaled for production at industrially relevant scales. Such ultrasensitive UV detectors have a wide range of possible applications including secure space-to-space communications, pollution monitoring, water sterilization, flame sensing, and early missile plume detection.[17−19]

Figure 1a is the three-dimensional (3D) schematic illustration of the hybrid phototransistor. The structure of the 10-decyltrichlorosilane SAM used in this study is provided in Supporting Information 1, Figure S1. The channel of the phototransistor, consisting of a monolayer graphene sheet decorated with ZnO QDs, is placed on top of a $SAM/SiO_2/Si$ wafer (see Supporting Information 2 for detailed procedure for synthesis and deposition of ZnO QDs on SAM supported graphene channel). Figure 1b illustrates the charge transport process in the hybrid phototransistor when placed under UV illumination, and the molecular structure of the SAM. Figure 1c shows optical microscopy (left) and scanning electron microscopy (right) images of the CVD grown monolayer graphene in contact with gold electrodes, forming the phototransistor. The Raman spectra of the graphene transferred to the SAM/SiO_2 before and after deposition of ZnO QDs are shown in Figure 1d. For the pristine graphene on SAM, the absence of a D band peak (~1350 cm^{-1}) in the Raman spectra confirms the high quality and defect-free nature of the graphene sample.[20] The 2D peak (~2675 cm^{-1}) is also spectrally sharp and its intensity is about three times greater than that of the G peak (~1583 cm^{-1}), which are characteristics of monolayer graphene.[21] After deposition of ZnO QDs, a small D peak (~1338 cm^{-1}) appeared in the Raman spectrum (red curve), which is due to additional disorder/defects introduced during the deposition of QDs.[22,23] Ellipsometry analysis gave an average thickness of the SAM of ~1.3 ± 0.1 nm on the SiO_2/Si Wafer. Transmission electron microscopy (TEM) image and photoluminescence (PL) spectrum of the ZnO QDs are provided in Supporting Information 2, Figure S2. The X-ray diffraction (XRD) and optical absorption analysis of the ZnO decorated graphene can be found in Supporting Information 2, Figure S3.

Figure 2a shows the channel resistance of the pristine graphene on SAM, and the ZnO QDs-graphene on SAM as a function of backgate voltage (V_{BG}) measured under dark environment. The Dirac point V_D (i.e., the charge neutrality point) of the pristine graphene on SAM was initially at 23.6 V due to doping effects from the transfer process and the substrate. After deposition of the ZnO QDs on the device, the V_D was shifted to about 1.8 V, consistent with a slightly higher work function of ZnO QDs as compared to graphene, and the electron carrier mobility (see Methods in Supporting Information) decreased from ~10,800 to ~6,700 $cm^2\ V^{-1}\ s^{-1}$ due to the additional disorder/defects introduced by the QDs.[22,23] The carrier mobility of our hybrid phototransistor is almost 1 order of magnitude higher than that of a control device without the SAM (Supporting Information 3, and Figure S4) for which the mobility before and after deposition of ZnO QDs were measured to be ~1,120 and ~630 $cm^2\ V^{-1}\ s^{-1}$, respectively. Figure 2b shows the channel resistance of our hybrid phototransistor as a function of V_{BG} under varying illuminating power. The illumination causes the Dirac point to shift to lower values of V_{BG}, which is due to transfer of photogenerated electrons from the ZnO QDs to the graphene channel (photodoping effect). For a more detailed analysis of the channel resistance, we plot the channel resistance as a function of illuminating power and back-gate voltage, as shown in Figure 2c. From this data, the shift of V_D as a function of illuminating power is extracted. For a low illuminating power, the photodoping induced shift of V_D can reach to ~1.9 V/pW,

DOI: 10.1021/acs.nanolett.5b00380
Nano Lett. 2015, 15, 3787−3792

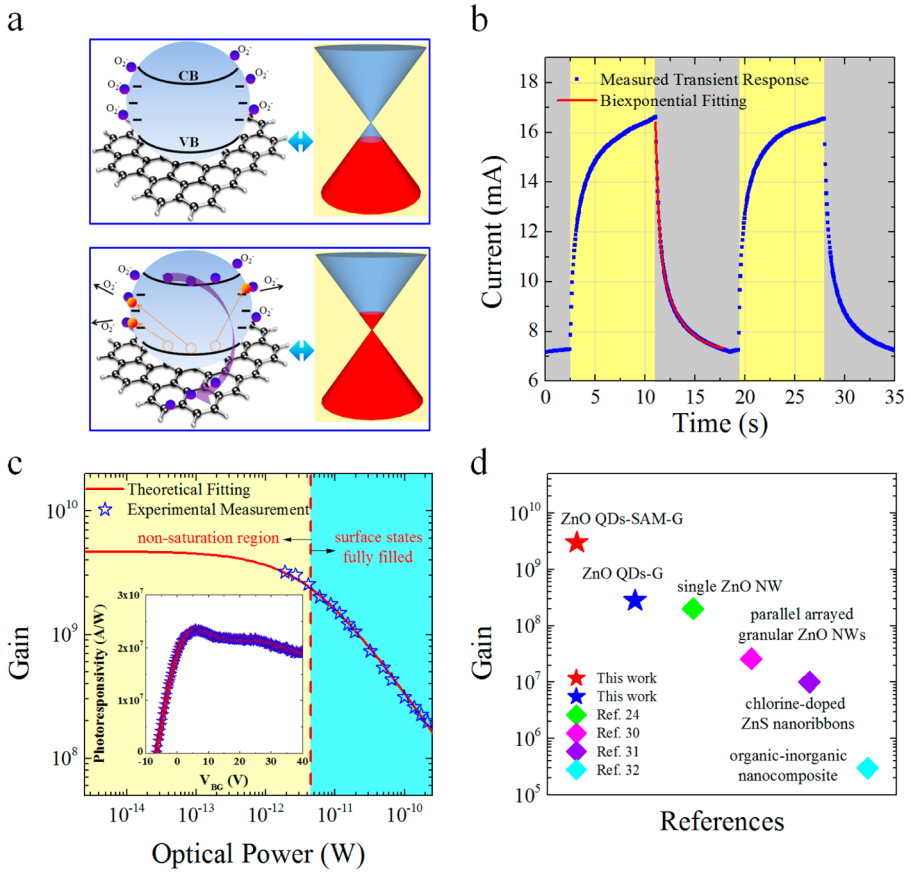

Figure 4. (a) Schematic illustration of the mechanism that contributes to the ultrahigh photoresponsivity of the hybrid phototransistor. (b) Transient response of the device for a excitation at wavelength of 335 nm (power: 138 pW). The red curve is the best-fitting for the data obtained with a biexponential decay function. (c) Photoconductive gain versus illuminating power, showing the high sensitivity of the phototransistor. The transistor exhibits a gain of ~3 × 10^9 for an illuminating power of 1.9 pW and shows a progressive decrease with increasing illuminating power due to the saturation of the surface states and reduced average lifetime of holes. The inset shows the photoresponsivity of our device as a function of the back-gate voltage, showing that the photoresponsivity of the detector can be directly controlled by the applied back-gate potential and can be tuned from ~2.4 × 10^7 A/W to 0. The measurement was performed for an excitation at wavelength of 335 nm with a power of ~138 pW. (d) Photoconductive gain for the ZnO QDs-SAM-G device is compared to a baseline ZnO QDs-G device without the SAM and other published reports on UV photodetectors.

demonstrating the high photosensitivity of our device at low illuminating power intensity. As the illuminating power increases, the V_D shift per unit optical power decreases, indicating reduced sensitivity for higher illuminating intensity. This is due to the reduced photodoping effect that originates from the saturation of surface trapped holes and reduced average lifetime of the holes at high illuminating intensity. The detailed analysis of this mechanism will be provided later.

The photocurrent as a function of source-to-drain bias (V_{DS}) is shown in Figure 3a, which reveals that the photocurrent depends linearly on the bias voltage V_{DS}. The photoresponsivity spectrum of the hybrid phototransistor, defined as the photocurrent per unit incident optical power, is shown in Figure 3b. For comparison, we also include the photoresponsivity spectra of a Si-avalanche photodiode (APD), a GaN photodetector, and a photomultiplier tube (PMT). Remarkably, the maximum photoresponsivity of our device with zero gate bias can reach to ~1.1 × 10^8 A/W in the UV region, which is at least 7 orders of magnitude higher than those of Si-APD and GaN photodetectors and is even 10 times higher than that of PMTs. Notably our device provides an excellent UV to visible rejection ratio (~10^3) that is 3 orders of magnitude higher than that of the PMT. The high photoresponsivity of our hybrid phototransistor is attributed to the high photoconductive gain that originates from the recirculation of electrons in the graphene channels within the lifetime of the photogenerated holes, which can be understood by referring to the carrier dynamics in the device, which is illustrated in Figure 4a.

It is well established that oxygen molecules adsorb onto oxide surfaces and capture the free electrons present in n-type metal oxide semiconductors, [O_2(g) + e^- → O_2^-(ad)], forming a low-conductivity depletion layer near the surface of ZnO, as shown in the top panel of Figure 4a.[24−26] For ZnO QDs, there is usually a high density of hole-trap states on the surface due to its high surface-to-volume ratio,[24] and this is in good agreement with the photoluminescence spectrum measured for the as-prepared ZnO QDs (Supporting Information 2, Figure S2b). When illuminated with photon energy larger than the bandgap of ZnO, electron−hole pairs are generated and soon separated with the holes trapped at the surface (due to the potential slope near the surface due to band bending), leaving behind unpaired electrons that quickly transfer to the graphene channel and are collected by the drain by means of the source-drain voltage. The trapped holes recombine with negatively charged oxygen ions and neutral oxygen molecules are then desorbed from the

DOI: 10.1021/acs.nanolett.5b00380
Nano Lett. 2015, 15, 3787−3792

surface of the ZnO QDs [O_2^-(ad) + $h^+ \rightarrow O_2$(g)], as shown in the bottom panel of Figure 4a. The effect of the oxygen molecule adsorption−desorption process was verified by measuring the photoresponse of the device under constant nitrogen flow (Supporting Information 4, Figure S5). The transit time of the electrons in the graphene channel is very short due to the graphene's high carrier mobility as well as the short channel length (20 μm for our device), while the surface oxygen molecule adsorption−desorption process usually results in a relatively long lifetime of the holes.[27] This leads to electron replenishment from the negative biased source as soon as an electron reaches the positive biased drain. Accordingly, multiple electrons will circulate in the graphene channel following a single electron−hole photogeneration event, leading to a very high photoconductive gain. It is to be noted that oxygen and water molecules present in air will also physisorb at the graphene/SiO_2 interface and p-dope the graphene channel. However, as shown in Figure 2a the deposition of ZnO QDs results in a significant shift of the Dirac Point from 23.6 to 1.8 V due to the transfer of electrons from the ZnO QDs to the graphene, which compensates the doping effect of physisorbed oxygen at the graphene/SiO_2 interface. Therefore, the oxygen molecule adsorption/desorption process at the surface of the ZnO QDs plays a much more important role in the gain mechanism of this phototransistor.

It is important to note that the gain of our hybrid phototransistor is expected to be a function of the excitation light intensity due to the effect of the traps states on the surface of the ZnO QDs. At low intensity excitation, the holes, separated from photogenerated electron−hole pairs, will occupy the surface states, thus remaining trapped at the surface and will recombine with the negative charged oxygen molecules. However, as the light intensity increases and more electron−hole pairs are generated, the number of available hole-trap states present at the surface will be diminished. As the trap states are filled, the energy bands flatten and the extra electron−hole pairs recombine immediately after they are generated in the time scale of several tens of picoseconds.[28] Therefore, the extra electron−hole pairs that are generated (after the saturation of surface states) will not participate in the charge transfer process, and the average lifetime will be shortened. Because the carrier lifetime of the holes is related to the excitation light intensity as well as the available surface traps, it can be expressed as

$$T(P) = T_{\text{life}} \frac{1}{1 + \left(\frac{P}{P_0}\right)^n}$$

Where, T_{life} is the carrier lifetime at low excitation intensity, P is the excitation light intensity on the QDs, P_0 is the saturation light intensity on the QDs in which the all the surface states are filled, and n is a phenomenological fitting parameter. Thus, the free carrier concentration (N) in the ZnO QDs can be expressed as

$$N = \frac{\eta P}{h\nu} T(P) = \frac{\eta P}{h\nu} T_{\text{life}} \frac{1}{1 + \left(\frac{P}{P_0}\right)^n}$$

Where η is the internal quantum efficiency of the QDs and $h\nu$ is the photon energy of the excitation light. The gain can thus be deducted as

$$G = \frac{I_{\text{ph}} h\nu}{qPWL} = (\alpha q N V W) \frac{h\nu}{qPWL} = \alpha\eta \frac{T_{\text{life}}}{T_{\text{transit}}} \frac{1}{1 + \left(\frac{P}{P_0}\right)^n}$$

where α is the carrier transfer efficiency from ZnO QDs to the graphene channel, q is the elementary charge, W is the channel width, and $V = \mu V_{\text{DS}} L^{-1}$ is the carrier drift velocity in graphene with the carrier mobility μ and the sample length L. $T_{\text{transit}} = L^2 \mu^{-1} V_{\text{DS}}^{-1}$ is the carrier transit time in the graphene channel. For our device, with W = 90 μm, L = 20 μm, V_{DS} = 1.5 V, and μ = 6700 $cm^2\ V^{-1}\ s^{-1}$ T_{transit} is estimated to be ~0.4 ns. From the above expression derived for the gain, we conclude that under low power illumination ($P \ll P_o$), a very short transit time of the electrons in the graphene channel compared with the lifetime of the holes ($T_{\text{transit}} \ll T_{\text{life}}$) will result in a high gain for the device.

To quantitatively verify the above physical model for the gain, it is necessary to determine the carrier lifetime of the holes in the device. We measured the transient response of the hybrid phototransistor and the result is presented in Figure 4b. The decay trace can be approximately fitted by a biexponential function, from which the lifetime of the holes can be extracted as T_{life} = 2.3 s. This approach has been widely used and proved to be an efficient way to determine the carriers' lifetime.[22,24,29] It is noteworthy that the lifetime of the holes in the QDs (~2.3 s) is over 9 orders of magnitude greater than the electron transit time in the FET channel (~0.4 ns). On the basis of the measurements of the response time scale, T_{transit} and T_{life}, we verify that our experimentally observed gain is in good agreement with the theoretical gain, as shown in Figure 4c. The device demonstrated a maximum gain of 3×10^9 for an illuminating power of 1.9 pW and showed a progressive decrease with increasing illuminating power due to the saturation of the surface states and reduced average lifetime of holes. The solid red curve is the best fitting for the measured gain with fitting parameters: P_0 = 4.5 pW, n = 0.83, and $\alpha\eta$ = 81.7%. The theoretical calculation predicts that a maximum gain as high as ~4.7×10^9 can be achieved for excitation light with power <10 fW. Such a high gain suggests that our hybrid phototransistor could be used for single-photon detection. For comparison, the gain measured for a control device without SAM fabricated using the same processing technique and the gain reported for other high-performance UV photodetectors in recent references[30−32] has been presented in Figure 4d. Indeed, our hybrid UV phototransistors achieved the highest gain as compared to all other types of UV photodetectors. The maximum gain-bandwidth product of our hybrid phototransistor is on the order of 3.3×10^8 Hz (given by the product of 4.7×10^9 gain and ~0.07 Hz of 3 dB bandwidth).

Besides gain and photoresponsivity, the specific detectivity (D^*) is also one of the key figure-of-merits for a photodetector, which is expressed as

$$D^* = \frac{\sqrt{A \times \Delta f}}{\text{NEP}} \text{(Jones)}$$

where the NEP is the noise equivalent power in the unit of A/$Hz^{1/2}$, Δf is bandwidth in hertz, and A is the area of the device in cm^2. The noise level of our phototransistor under dark environment was measured to be ~2×10^{-3} $\Omega/Hz^{1/2}$, which sets the lower threshold limit of noise-equivalent power at ~1.4×10^{-16} W (see Supporting Information 5 and Figure S6). This yields a specific detectivity D^* of ~5.1×10^{13} Jones at 368 nm

DOI: 10.1021/acs.nanolett.5b00380
Nano Lett. 2015, 15, 3787−3792

at room temperature. The detectivity comparisons of our hybrid phototransistor with commercial photodetectors and various other types of photodetectors (see Supporting Information 6, Figure S7 and Table S1) demonstrate the outstanding sensitivity of this device. For commercial photodetectors, only the photomultiplier tube (PMT) has a higher detectivity than our device (in the UV region). However, as previously discussed in the introduction, PMT devices have several limitations that include its large size, high cost, complexity, and the requirement for high-voltage power supply (typically >1 kV). It should be noted that although our hybrid UV phototransistor achieves the highest gain reported to date, its detectivity is lower than commercial PMT due to the extremely high conductivity of the SAM supported graphene channel, which increases the dark current in the device.

In addition to the high sensitivity and detectivity, another advantage of our hybrid phototransistor is that its gain can be tuned by varying the back-gate voltage, as shown in the inset of Figure 4c. A maximum responsivity as high as $\sim 2.4 \times 10^7$ A/W was obtained for V_{BG} = 5.6 V for an excitation at wavelength of ~335 nm with a power intensity of ~138 pW. By tuning the Fermi energy close to the Dirac point at V_{BG} = −6.6 V, the responsivity can be reduced to zero. Such tunability allows control of the on−off state of the photodetector as well as adjustment of the required gain, which is useful for pixelated imaging applications where the implementation of nanoscale local gates enables a locally tunable photoresponse.

■ ASSOCIATED CONTENT

Supporting Information

Details of the material synthesis, device fabrication and characterization, and detectivity comparisons are given in this section. The Supporting Information is available free of charge on the ACS Publications website at DOI: 10.1021/acs.nanolett.5b00380.

■ AUTHOR INFORMATION

Corresponding Authors

*E-mail: (N.A.K.) koratn@rpi.edu.

*E-mail: (S.S.) sawyes@rpi.edu.

Author Contributions

D.S. and J.G. contributed equally in this manuscript.

Notes

The authors declare no competing financial interest.

■ ACKNOWLEDGMENTS

N.A.K. acknowledges funding support from the USA National Science Foundation (Awards CMMI 1234641 and CMMI 1435783). J. L. acknowledges funding support from the USA National Science Foundation (Award: CMMI 1463083). S. S. acknowledges funding support from the Engineering Research Centers Program of the National Science Foundation under NSF Cooperative Agreement No. EEC-0812056 and in part by New York State under NYSTAR contract C130145.

■ REFERENCES

(1) Liu, C.-H.; Chang, Y.-C.; Norris, T. B.; Zhong, Z. *Nat. Nanotechnol.* **2014**, *9*, 273−278.

(2) Rumyantsev, S.; Liu, G.; Shur, M. S.; Potyrailo, R. A.; Balandin, A. A. *Nano Lett.* **2012**, *12*, 2294−2298.

(3) Mohanty, N.; Berry, V. *Nano Lett.* **2008**, *8*, 4469−4476.

(4) Geim, A. K.; Novoselov, K. S. *Nat. Mater.* **2007**, *6*, 183−191.

(5) Schwierz, F. *Nat. Nanotechnol.* **2010**, *5*, 487−496.

(6) Bolotin, K. I.; Sikes, K. J.; Hone, J.; Stormer, H. L.; Kim, P. *Phys. Rev. Lett.* **2008**, *101*, 096802.

(7) Chen, F.; Xia, J.; Tao, N. *Nano Lett.* **2009**, *9*, 1621−1625.

(8) Chen, J. H.; Jang, C.; Adam, S.; Fuhrer, M. S.; Williams, E. D.; Ishigami, M. *Nat. Phys.* **2008**, *4*, 377−381.

(9) Chen, J. H.; Jang, C.; Xiao, S. D.; Ishigami, M.; Fuhrer, M. S. *Nat. Nanotechnol.* **2008**, *3*, 206−209.

(10) Ni, Z. H.; Ponomarenko, L. A.; Nair, R. R.; Yang, R.; Anissimova, S.; Grigorieva, I. V.; Schedin, F.; Blake, P.; Shen, Z. X.; Hill, E. H.; Novoselov, K. S.; Geim, A. K. *Nano Lett.* **2010**, *10*, 3868−3872.

(11) Ishigami, M.; Chen, J. H.; Cullen, W. G.; Fuhrer, M. S.; Williams, E. D. *Nano Lett.* **2007**, *7*, 1643−1648.

(12) Gao, J.; Chow, P. K.; Thomas, A. V.; Lu, T.-M.; Borca-Tasciuc, T.; Koratkar, N. *Appl. Phys. Lett.* **2014**, *105*, 123108.

(13) Lafkioti, M.; Krauss, B.; Lohmann, T.; Zschieschang, U.; Klauk, H.; von Klitzing, K.; Smet, J. H. *Nano Lett.* **2010**, *10*, 1149−1153.

(14) Liu, Z.; Bol, A. A.; Haensch, W. *Nano Lett.* **2011**, *11*, 523−528.

(15) Wang, X.; Xu, J.-B.; Wang, C.; Du, J.; Xie, W. *Adv. Mater.* **2011**, *23*, 2464−2468.

(16) Petrone, N.; Dean, C. R.; Meric, I.; van der Zande, A. M.; Huang, P.; Wang, L.; Muller, D.; Shepard, K. L.; Hone, J. *Nano Lett.* **2012**, *12*, 2751−2756.

(17) Liu, S.; Ye, J.; Cao, Y.; Shen, Q.; Liu, Z.; Qi, L.; Guo, X. *Small* **2009**, *5*, 2371−2376.

(18) Zhang, D.; Gan, L.; Cao, Y.; Wang, Q.; Qi, L.; Guo, X. *Adv. Mater.* **2012**, *24*, 2715−2720.

(19) Li, H.-G.; Wu, G.; Shi, M.-M.; Yang, L.-G.; Chen, H.-Z.; Wang, M. *Appl. Phys. Lett.* **2008**, *93*, 153309.

(20) Wang, Y.; Ni, Z.; Yu, T.; Shen, Z.; Wang, H.; Wu, Y.; Chen, W.; Wee, A. T. S. *J. Phys. Chem. C* **2008**, *112*, 10637.

(21) Dresselhaus, M. S.; Jorio, A.; Hofmann, M.; Dresselhaus, G.; Saito, R. *Nano Lett.* **2010**, *10*, 751−758.

(22) Konstantatos, G.; Badioli, M.; Gaudreau, L.; Osmond, J.; Bernechea, M.; de Arquer, F. P. G.; Gatti, F.; Koppens, F. H. L. *Nat. Nanotechnol.* **2012**, *7*, 363−368.

(23) Guo, W.; Xu, S.; Wu, Z.; Wang, N.; Loy, M. M. T.; Du, S. *Small* **2013**, *9*, 3031−3036.

(24) Soci, C.; Zhang, A.; Xiang, B.; Dayeh, S. A.; Aplin, D. P. R.; Park, J.; Bao, X. Y.; Lo, Y. H.; Wang, D. *Nano Lett.* **2007**, *7*, 1003−1009.

(25) Shao, D.; Yu, M.; Sun, H.; Hu, T.; Sawyer, S. *Nanoscale* **2013**, *5*, 3664−3667.

(26) Fan, Z.; Wang, D.; Chang, P.-C.; Tseng, W.-Y.; Lu, J. G. *Appl. Phys. Lett.* **2004**, *85*, 5923−5925.

(27) Robel, I.; Bunker, B. A.; Kamat, P. V. *Adv. Mater.* **2005**, *17*, 2458−2463.

(28) Fonoberov, V. A.; Balandin, A. A. *J. Nanoelectron. Opotelectron.* **2006**, *1*, 19−38.

(29) Sun, Z.; Liu, Z.; Li, J.; Tai, G.-A.; Lau, S.-P.; Yan, F. *Adv. Mater.* **2012**, *24*, 5878−5883.

(30) Liu, X.; Gu, L.; Zhang, Q.; Wu, J.; Long, Y.; Fan, Z. *Nat. Commun.* **2014**, *5*, 4007.

(31) Yu, Y.; Jie, J.; Jiang, P.; Wang, L.; Wu, C.; Peng, Q.; Zhang, X.; Wang, Z.; Xie, C.; Wu, D.; Jiang, Y. *J. Mater. Chem.* **2011**, *21*, 12632−12638.

(32) Guo, F.; Yang, B.; Yuan, Y.; Xiao, Z.; Dong, Q.; Bi, Y.; Huang, J. *Nat. Nanotechnol.* **2012**, *7*, 798−802.

DOI: 10.1021/acs.nanolett.5b00380
Nano Lett. 2015, 15, 3787−3792